Flow-fiber coupled injection molding simulations with non-uniform fiber concentration effects

Tianyi Li, Jean-François Luyé

Flow-fiber coupled injection molding simulations with non-uniform fiber concentration effects

Tianyi Li[a,*], Jean-François Luyé[a]

[a]*Promold, 42 rue Boursault, 75017 Paris, France*

Abstract

We propose to account for non-uniform fiber concentration effects in a novel fiber-flow coupled injection molding simulation framework. The rheological properties of fiber suspensions are characterized by an optimal scalar viscosity defined by a minimization principle. Comprehensive theoretical analyses are carried out to gain further physical insights into this approximate orientation-dependent model. The flow-induced fiber orientation and migration are numerically computed and then injected into the constitutive equation at every time-step. Based on careful post-processing of the obtained kinematics and fiber evolution, simulation results on a center-gated disk suggest a stronger coupling behavior due to a spatially-varying concentration. This multiphysics coupling leads to a further improvement in terms of fiber orientation prediction compared with experimental results.

Keywords: Fiber orientation, Fiber concentration, Anisotropy, Multiphysics coupling, Injection molding simulation

1. Introduction

An accurate prediction of the final fiber orientation is crucial for injection-molded fiber reinforced composites. Fiber-induced material anisotropy leads to non-homogeneous effective thermomechanical properties [1] and may also impact the fatigue, damage and ultimate failure mechanisms of these composites [2, 3]. The fiber microstructure evolution during the molding process is greatly governed by complex flows produced by an anisotropic non-Newtonian suspension [4]. More advanced theoretical models and numerical methods need to be developed to correctly characterize the flow kinematics and flow-induced filler evolution.

Flow-fiber coupled simulations are identified by a mutual exchange of information between the flow kinematics and the fiber evolution via an anisotropic constitutive model, see [5, 6] for a review and [7–14] for some more recent updates on this subject. According to the dimensional analysis of [15], such fiber-dependent rheological equations are needed especially at high fiber concentration regime [16] and for chunky geometries [17]. Nevertheless, flow-fiber coupling is still not gaining popularity in the injection molding community, probably because such constitutive models are not yet implemented in a majority of commercial simulation software for production use.

In our previous work [18], we developed the optimal scalar viscosity model as an approximation to the homogenization-based anisotropic fiber-induced viscosity tensor and successfully implemented it in

*Corresponding author

Email addresses: tianyi.li@promold.fr; tianyikillua@gmail.com (Tianyi Li), jfluye@promold.fr (Jean-François Luyé)

the Moldflow Insight API framework [19]. The effective rheological behavior of the fiber suspension is thus characterized by a scalar value depending on the microstructure and the current deformation mode. Independently, a similar idea [13] has emerged recently with their particular applications to compression molding simulations. In this paper, we propose in Section 2 to carry out a comprehensive theoretical analysis of this orientation-dependent scalar viscosity, with a focus on its approximate nature. The objective is to determine if the model can indeed be used with confidence in real injection molding simulations, with a correct rheological modeling and a controllable approximation error.

Another important aspect of this work is the consideration of non-uniform fiber concentration effects in such flow-fiber coupling framework. Admittedly, filler concentration is already accounted for in these micromechanical constitutive models in particular via their particle number coefficient, see [5]. However, only non-uniform fiber orientation is taken into account in most fiber-flow coupled simulations reported in the literature. The fiber orientation state is often computed by various orientation models based on the work of [20, 21]. The viscosity function is then updated at every time step using the current calculated fiber orientation, with the implicit assumption that fiber concentration is spatially homogeneous and is at its nominal value. The effect of a non-homogeneous concentration distribution in a flow-fiber coupling context has been considered for instance in [22] in a simplifying framework. Inter-fiber interaction [21] is not taken into account and the results are reported based on an empirical fiber volume fraction profile prescribed in the gapwise direction that remains constant as the flow advances.

However, fiber migration phenomenon is also known to take place during injection molding, resulting in a non-uniform fiber concentration both in the thickness direction and along the flow path, see for instance [23–26]. According to a recent work [26], such effect could induce an important influence on the material constitutive behaviors especially in the core region, where fiber concentration could be significantly higher than the nominal value. The authors also suggest a coupling between fiber orientation and concentration computations to better predict the final fiber microstructure.

This multiphysics coupling is achieved in this paper via the above orientation-and concentration-dependent optimal scalar viscosity. Contrary to [22], the flow-fiber coupling is now accompanied additionally by a fiber migration model that computes numerically a spatially and temporarily varying fiber volume fraction, see Fig. 1. By coupling separately fiber orientation and concentration with the flow equations, it induces automatically an indirect relation between orientation and concentration. More information on the fiber orientation and concentration models used in this paper will also be specified at the end of Section 2, where more details on our flow-fiber coupled simulation framework are given. The idea of using a non-uniform fiber concentration computed by specific numerical methods has also emerged recently in [27] for a better prediction of the stress response during rheological measurements. The objective of this paper is thus to extend this concept to a three-dimensional non-Newtonian flow problem.

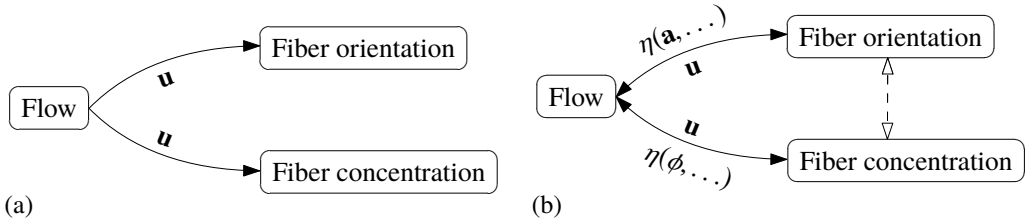

Figure 1: (a) Standard uncoupled solving procedure (b) Flow-fiber coupling with an orientation- and concentration-dependent viscosity.

The center-gated disk geometry along with its characteristic radially diverging flow is a well-studied

benchmark problem representative of injection molding. In Section 3, numerical simulations are carried out in order to validate the proposed coupled simulation framework against the well-documented experimental results reported in [10, 24, 28]. The objective is to numerically illustrate the effect of a non-uniform fiber concentration on the flow kinematics, the rheological behavior and the final fiber orientation. Conclusions and future research directions drawn from the numerical studies are indicated in Section 4.

2. Flow-fiber coupled injection molding simulation framework

2.1. Anisotropic fiber-induced constitutive behaviors

The point of departure of flow-fiber coupled simulations are the so-called anisotropic fluid constitutive models, cf. for instance [5, 15, 29] and references therein for a review on this subject. Using a micromechanical approach, these models provide a theoretical characterization of the macroscopic rheological behaviors of those filler suspensions. For typical short or long fiber-reinforced thermoplastics with a relatively large aspect ratio ($r > 20$ for example) and a high concentration level (for instance when $\phi r > 1$ where ϕ is the fiber volume concentration), the anisotropic constitutive behavior induced by the presence of these immersed fibers can be reasonably predicted by the model proposed by [30], where the macroscopic stress tensor $\boldsymbol{\sigma}$ reads

$$\boldsymbol{\sigma} = -p\mathbf{I} + 2\mathbb{V}\mathbf{D} = -p\mathbf{I} + 2\eta\mathbf{D} + 2\eta N_{\mathrm{p}}\mathbb{A}\mathbf{D}. \tag{1}$$

In (1), p is the pressure, $\mathbf{I}$ is the 2nd order identity tensor, $\mathbf{D} = \frac{1}{2}\,\mathrm{dev}(\nabla\mathbf{u} + \nabla^{\mathsf{T}}\mathbf{u})$ is the deviatoric strain rate tensor (deviatoric part of the symmetrized velocity gradient), η refers to the viscosity of the matrix (suspending fluid without fibers) and finally $\mathbb{A}$ designates the 4th-order fiber orientation tensor introduced in [31]. From a mathematical point of view, the viscosity $\mathbb{V}$ of the suspension modeled by (1) is now a 4th-order tensor

$$\mathbb{V} = \eta(\mathbb{I} + N_{\mathrm{p}}\mathbb{A}), \tag{2}$$

with $\mathbb{I}$ the 4th order identity operator. The 4th-order viscosity tensor $\mathbb{V}$ is in general anisotropic due to the presence of fibers.

As a scalar measure, the particle number N_{p} introduced by [15] that is present in (1) and (2) characterizes the importance of the anisotropic contribution of fibers to the overall viscosity. It is a function of the microstructural properties of the fiber suspension, and in particular the geometric shape (aspect ratio r) of fibers and the fiber volume fraction ϕ. For very dilute suspensions as $\phi \to 0$, the particle number N_{p} is also expected to become vanishingly small $N_{\mathrm{p}} \to 0$, and one recovers the fiber-independent matrix viscosity. In the anisotropic fluid models developed for dilute suspensions such as [32], the particle number coefficient is linearly proportional to the volume fraction. In the meanwhile, experimental findings indicate a much more rapid increase of N_{p} as ϕ becomes larger, cf. for instance [16] for a recent discussion on the subject. For this reason, the N_{p} expression proposed by [30] seems more appropriate for typical fiber-reinforced thermoplastics. For a specific volume fraction ϕ and fiber aspect ratio r, the value of N_{p} is given by the following expression

$$N_{\mathrm{p}} = \frac{\phi r^2(2 - \phi/A)}{4(\ln 2r - 1.5)(1 - \phi/A)^2}, \tag{3}$$

where A is referred to as the maximum allowable volume fraction in [30]. In this paper however, it is merely regarded a dimensionless fitting parameter. With a standard fiber aspect ratio $r = 25$, the N_{p} expression (3) is illustrated in Fig. 2 with two values of the A parameter. For comparison, the traditional linear theory of [32] for dilute suspensions is also indicated. For the material that will be considered in Section 3 (Valox 420, PBT-GF30), the N_{p} expression of [30] predicts a larger fiber-induced anisotropic contribution at its nominal

mass fraction of 30%. We can also observe an increase of the N_p value as the A parameter becomes smaller. Contrary to previous work in the literature, here the fiber volume fraction ϕ in the expression of N_p will not be considered as a constant (its nominal value $\overline{\phi}$) but a spatially and temporarily variable that will be solved along with fiber orientation.

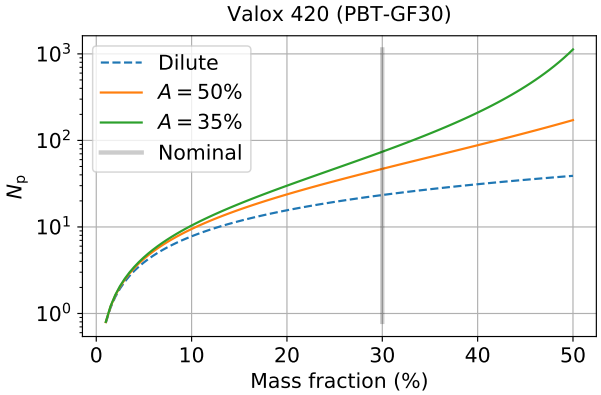

Figure 2: Particle number N_p given by [30] as a function of the mass fraction for two values of the A parameter.

2.2. *Fiber-dependent optimal scalar viscosity model*

Ideally, the anisotropic fiber-induced 4th-order viscosity tensor (2) can be used to couple flow equations and fiber evolution models in an actual injection molding simulation, see [6, 7, 10, 11, 33] among others. However, probably due to numerical and implementation difficulties it is not yet possible for several widely used commercial injection molding simulation software. For instance, in the Moldflow Insight API framework described in [19], only a *scalar* user-defined viscosity function can be implemented. Due to this reason, in [13, 18] several authors independently proposed a scalar viscosity model designed to *approximate* the original 4th-order viscosity model (2). Compared to standard generalized Newtonian models such as the Cross model [34] frequently used in injection molding simulations, the "optimal scalar viscosity model" of [18] or the "informed isotropic viscosity model" proposed by [13] is now a function of the complete deviatoric strain rate tensor $\mathbf{D}$ (and not just its magnitude $\|\mathbf{D}\|$). The objective is hence to provide an adequate scalar viscosity measure, depending on the current fiber orientation state and the deformation mode.

Motivated by the fact that the 4th-order viscosity tensor $\mathbb{V}$ is perceived by the stress tensor via its application $\mathbb{V}\mathbf{D}$ on the deviatoric strain rate tensor $\mathbf{D}$, in [18] the optimal scalar viscosity η_* is defined such that the scalar multiplication $\eta_*\mathbf{D}$ is as close as possible to $\mathbb{V}\mathbf{D}$

$$\boldsymbol{\sigma}_* = -p\mathbf{I} + 2\eta_*\mathbf{D} \approx \boldsymbol{\sigma} = -p\mathbf{I} + 2\mathbb{V}\mathbf{D} \implies (\eta_*\mathbf{D} - \mathbb{V}\mathbf{D}) \to \min . \tag{4}$$

Since the resulting 2nd-order tensor $\mathbb{V}\mathbf{D}$ is not guaranteed to be invertible nor positive-definite, the most natural scalar approximation error is using the standard Euclidian (Frobenius) norm (square root of the sum of all components squared). From (4), since the volumetric part of the stress tensor can be absorbed by the pressure p, it now seems more adequate to minimize only the *deviatoric* part the approximation error

$$e_{\eta_*} = \|\mathrm{dev}(\eta_*\mathbf{D} - \mathbb{V}\mathbf{D})\| = \min_{\nu} \|\mathrm{dev}(\nu\mathbf{D} - \mathbb{V}\mathbf{D})\| , \tag{5}$$

where $\mathrm{dev}\,\mathbf{D}$ designates the deviatoric part $\mathrm{dev}\,\mathbf{D} = \mathbf{D} - \left(\frac{1}{3}\,\mathrm{tr}\,\mathbf{D}\right)\mathbf{I}$ of a 3-dimensional 2nd-order tensor (tr is the trace operator). Using the definition of the 4th-order viscosity tensor (2), a direct minimization of (5)

(by differentiating $e^2_{\eta_*}$ with respect to $\mathbf{D}$) leads to the following optimal scalar viscosity approximating the 4th-order anisotropic viscosity when $\mathbf{D} \neq \mathbf{0}$

$$\eta_* = (1 + N_\mathrm{p}\mathsf{a}_*)\eta \quad \text{with} \quad \mathsf{a}_* = \frac{\mathbf{D} \cdot \mathbb{A}\mathbf{D}}{\|\mathbf{D}\|^2}, \tag{6}$$

where the dot "$\cdot$" refers to the standard Euclidian inner product. The same expression of η_* is found as in [18], even though here in (5) only the deviatoric part is being minimized. This is due to the fact that the strain rate tensor $\mathbf{D}$ is assumed to be deviatoric. Note that the motivation as well as the final expression of our optimal scalar viscosity are extremely similar in essence to the "informed isotropic viscosity" proposed in [13, 35].

Optimal scalar viscosity for typical deformation modes and fiber orientation states. As suggested in [18], some additional theoretical studies of the proposed model (6) are now carried out here to gain further physical insights. The "optimal scalar" a_* of the 4th-order fiber orientation tensor in (6) is regarded as a flow-fiber coupling factor that adapts our fiber-dependent viscosity to the current deformation mode. Its value for two particular orientation states (fully random and perfectly unidirectional (UD) orientation) under several typical flow types is indicated in Fig. 3 for two commonly used closure models (the ORT model of [36] and the quadratic model reviewed in [31]) for the 4th-order fiber orientation tensor. Note that we do not observe much differences between the ORT closure and the IBOF model [37]. For visualization purposes, the zero value is replaced by an extremely short bar that can be barely seen in Fig. 3.

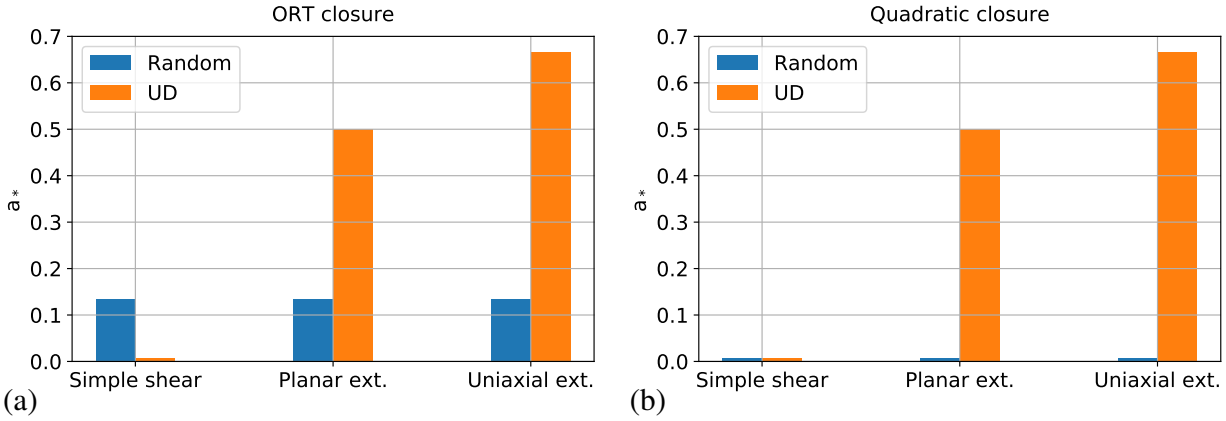

Figure 3: Coupling factor a_* for two particular orientation states under several typical flow types: (a) using the ORT closure and (b) using the quadratic closure.

From Fig. 3 (a), while a completely random fiber orientation state gives always the same value $\frac{2}{15}$ for all deformation types, for the unidirectional orientation state (UD) the coupling factor behaves anisotropically and ranges from 0 for simple shear, up to $\frac{2}{3}$ when the uniaxial elongational flow is considered. The importance of the closure model used to compute $\mathbb{A}$ is also obvious from Fig. 3, where the random fiber orientation state always leads to a vanishing value of a_* when using the quadratic closure as is the case in [38]. For simple shear situations this seems to contradict experimental findings [39] where the effective viscosity of a randomly orientated suspension should be higher than the case when fiber are completely orientated along the shear direction. In [13] it has been shown that the optimal scalar viscosity model is also capable of reproducing the overshoot phenomenon as fibers gradually reorient toward the shear direction.

The TUB triangle proposed by [40] provides a concise parametrization of all possible fiber orientation states using the two major principal values $a_1 \geq a_2$ of the 2nd-order tensor $\mathbf{a}$, since the 3rd principal value

can be computed using the condition $\mathrm{tr}\,\mathbf{a} = a_1 + a_2 + a_3 = 1$. For a given deformation mode $\mathbf{D}$, the variation of the coupling factor a_* can thus be illustrated on this orientation space to better understand the behavior of the proposed model (6). An additional approximation error measure similar to (5) is defined for the dimensionless coupling factor in order to quantify the discrepancy induced by the scalar model

$$e_{\mathsf{a}_*} = \|\mathrm{dev}(\mathsf{a}_*\mathbf{D} - \mathbb{A}\mathbf{D})\| = \min_a \|\mathrm{dev}(a\mathbf{D} - \mathbb{A}\mathbf{D})\| \quad \text{for } \|\mathbf{D}\| = 1. \tag{7}$$

By comparing (5) and (7), the actual approximation error on the viscosity e_{η_*} can be recomputed from e_{a_*} using $e_{\eta_*} = (N_\mathrm{p}\eta)e_{\mathsf{a}_*}$ for $\|\mathbf{D}\| = 1$. The additional norm condition on $\mathbf{D}$ leads to a unique normalized error since we have $e_{\mathsf{a}_*}(k\mathbf{D}) = k e_{\mathsf{a}_*}(\mathbf{D})$ for $k \in \mathbb{R}$. In Fig. 4, the coupling factor a_* as well as the dimensionless approximation error e_{a_*} are illustrated on the TUB orientation space for the uniaxial elongation case.

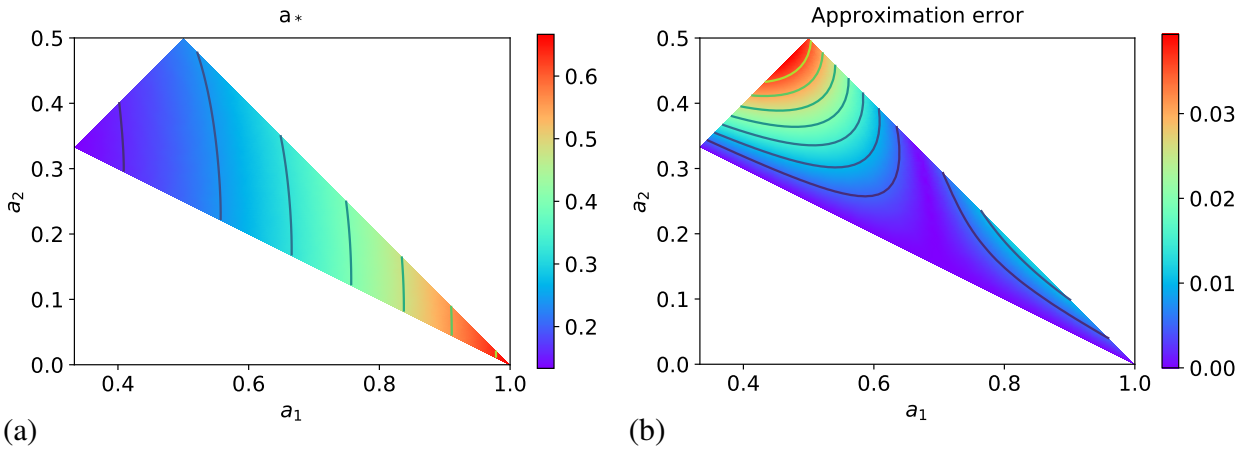

Figure 4: (a) Coupling factor a_* and (b) the dimensionless approximation error e_{a_*} on the TUB orientation space for uniaxial elongation.

Note that in Fig. 4 (a) the uniaxial extension direction coincides with the principal material direction corresponding to a_1. On the one hand, it can be verified that the flow-fiber coupling is maximum for the UD case $(a_1, a_2) = (1, 0)$ and minimum for the random orientation state $(a_1, a_2) = (\frac{1}{3}, \frac{1}{3})$. On the other hand, the largest approximation error measured by (7) in this particular case is less than 0.04, and is attained somewhere between the fully random state and the planar random state $(a_1, a_2) = (0.5, 0.5)$.

Remark 1. An approximation error of zero does not necessarily imply that the 4th-order viscosity tensor $\mathbb{V}$ is fully recovered by our optimal scalar approximation η_* at a given deformation mode $\mathbf{D}$. According to our error measure (5) and (7), it merely means the error $\eta_*\mathbf{D} - \mathbb{V}\mathbf{D}$ is *volumetric*, *i.e.* proportional to the identity matrix.

Anisotropy captured by the optimal scalar model. The anisotropy of the original 4th-order viscosity tensor (2) and the optimal scalar viscosity model (6) can be generally perceived as its directional dependence for different deformation modes $\mathbf{D}$, see for instance the UD situation in Fig. 3 (a) for 3 different $\mathbf{D}$'s. In [35], the author provides an excellent visualization of anisotropy for planar orientation states $a_3 = 0$ and a particular class of deformation modes. Here, a more general and mathematical approach is adopted to quantify the anisotropy of these models. The objective is to verify if the proposed scalar optimal viscosity model actually also possesses a similar anisotropic behavior.

Similarly for anisotropic elastic tensors, a scalar anisotropy index in the sense of [41] can also be defined for our anisotropic 4th-order viscosity / fiber orientation tensors (2). In this paper, the dimensionless anisotropic index A will be simply defined as the Euclidian distance

$$\mathsf{A} = \|\mathbb{A} - \mathbb{A}_{\text{iso}}\| \tag{8}$$

between the original 4th-order orientation tensor $\mathbb{A}$ and its closest isotropic projection $\mathbb{A}_{\text{iso}}$, see [42] for in particular its explicit expression.

Due to the scalar nature of the proposed viscosity model (6), its extent of anisotropy can only be quantified by the range (interval between the minimum and maximum values) of η_*, or equivalently of the dimensionless coupling factor a_*, as the deformation mode $\mathbf{D}$ varies. As is correctly noted by [35], the expression of a_* in (6) is nothing but the Rayleigh quotient associated with the corresponding 4th-order tensor $\mathbb{A}$. The optimal scalar viscosity can thus be regarded as an approximate eigenvalue at the deformation mode $\mathbf{D}$. Since the latter is required to be deviatoric $\operatorname{tr}\mathbf{D} = 0$, and we are only interested in the deviatoric part of the approximation error (7), it can be shown that the extreme values of a_* can be obtained by considering the following *unconstrained* symmetric eigenvalue problem

$$\mathbb{A}'\widehat{\mathbf{D}}_i = \lambda_i \widehat{\mathbf{D}}_i \quad \text{where} \quad \mathbb{A}' = \operatorname{dev} \circ \mathbb{A} \circ \operatorname{dev}, \tag{9}$$

where the eigen-deformation mode $\widehat{\mathbf{D}}_i$ is only required to be a symmetric 2nd-order tensor of dimension 6. The composition of two deviatoric operators keeps the symmetric nature of the problem and permits us to only analyze traceless deformation modes $\widehat{\mathbf{D}}_i$. Among the 6 eigenvalues extracted from (9), the volumetric mode $\widehat{\mathbf{D}}_{\text{vol}}$ for which $\operatorname{tr}\widehat{\mathbf{D}}_{\text{vol}} \neq 0$ as well as its corresponding zero eigenvalue $\lambda_{\text{vol}} = 0$ must be discarded. The other 5 eigenvalues

$$\lambda_{\max} = \lambda_1 \geq \lambda_2 \geq \lambda_3 \geq \lambda_4 \geq \lambda_5 = \lambda_{\min}$$

and their respective *traceless* and *orthonormal* (both thanks to symmetry) eigen-deformation modes $\widehat{\mathbf{D}}_i$ constitute the spectral decomposition of the deviatoric orientation tensor $\mathbb{A}'$. From standard mathematical arguments, it follows that our dimensionless flow-fiber coupling factor a_* can be regarded as the Rayleigh quotient associated with $\mathbb{A}'$, and achieves its maximal (resp. maximal) value of $\lambda_{\max}$ (resp. $\lambda_{\min}$) at the corresponding eigenmode $\widehat{\mathbf{D}}_{\max}$ (resp. $\widehat{\mathbf{D}}_{\min}$)

$$\mathsf{a}_*(\mathbf{D}) \in [\lambda_{\min}, \lambda_{\max}] \quad \text{and} \quad \mathsf{a}_*(\widehat{\mathbf{D}}_i) = \lambda_i \tag{10}$$

The numerical range $\max(\mathsf{a}_*) - \min(\mathsf{a}_*)$ of a_* can thus be computed through a standard symmetric eigenvalue analysis and can be used to measure the extent of anisotropy of the optimal scalar model. In practice, the 4th-order tensor $\mathbb{A}'$ can be readily represented by a symmetric 6×6 matrix using an *orthonormal* basis of the symmetric 2nd-order tensor space, see [40, 42].

In Fig. 5, the anisotropy index A defined in (8) for original 4th-order fiber orientation tensors and the numerical range of the optimal scalar coupling factor a_* are presented on the TUB orientation space. On the one hand, both A and the numerical range are 0 for the isotropic orientation state. This confirms the intuition that the tensor is directionally independent. On the other hand, anisotropy is well maximum for both the original and the optimal scalar models for the UD state, as expected. This shows that the proposed optimal scalar viscosity model successfully recovers the desired anisotropy from the original 4th-order tensor.

According to (10), for different orientation states (so different $\mathbb{A}'$) the maximum value of the coupling factor a_* is actually attained at different maximizing deformation modes $\widehat{\mathbf{D}}_{\max}$. In Tab. 1, three fiber orientation states are analyzed, where a typical orientation $(a_1, a_2) = (0.8, 0.15)$ in injection molding is also indicated. In such case, the deformation mode that actually maximizes a_* is a general elongational flow

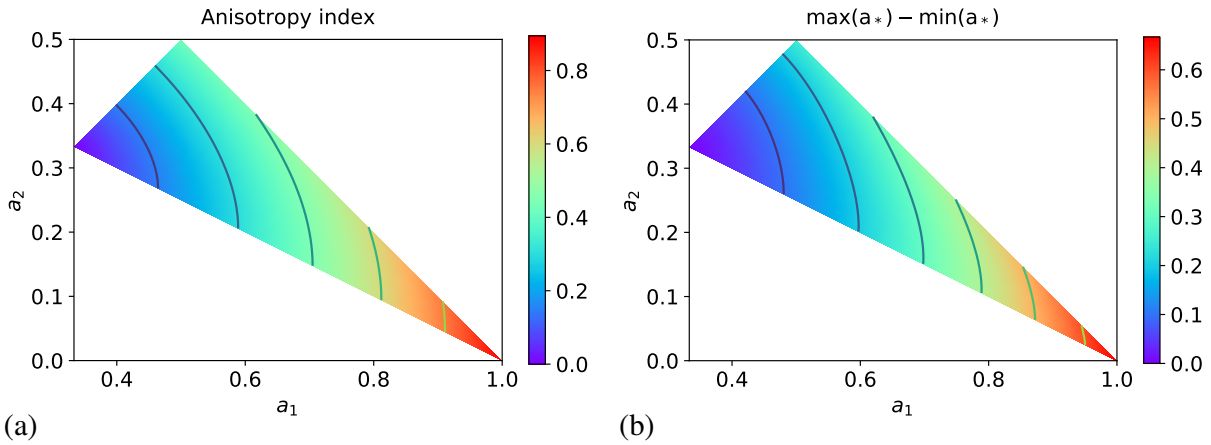

Figure 5: (a) Anisotropy index A of the 4th-order fiber orientation tensor; (b) numerical range $\lambda_{\max} - \lambda_{\min}$ of the proposed flow-fiber coupling factor a_*.

toward the $\mathbf{e}_1$ direction, and the contraction is slightly biased in the $\mathbf{e}_3$ direction. The UD case confirms what we have observed in Fig. 3 (a), while in the planar random state the maximum value of $\frac{1}{4}$ is actually achieved for any linear combination of the simple shear flow and the planar elongation in the same plane.

Table 1: Maximizing eigen-deformation modes $\widehat{\mathbf{D}}_{\max}$ for different fiber orientation states.

Fiber orientation state in TUB	$\widehat{\mathbf{D}}_{\max}$	$\max(\mathsf{a}_*)$
UD $(a_1, a_2) = (1, 0)$	Uniaxial elongation	$2/3$
Typical $(a_1, a_2) = (0.8, 0.15)$	General elongation $(D_{11}, D_{22}) \approx (0.82, -0.4)$	≈ 0.44
Planar random $(a_1, a_2) = (0.5, 0.5)$	Simple shear or planar elongation in the plane	$1/4$

Maximum approximation error of the optimal scalar model. In Fig. 4 (b), the dimensionless approximation error e_{a_*} given by (7) is calculated in the TUB orientation space for a particular deformation mode (uniaxial elongation). Based on the above outlined analogy between the coupling factor a_* regarded as the Rayleigh quotient of $\mathbb{A}'$ and the associated eigenvalue problem, we can actually compute the *maximum* approximation error that can be committed by an orientation state at a corresponding deformation mode. By decomposing the deviatoric strain rate tensor into the above principal basis $\mathbf{D} = D_i \widehat{\mathbf{D}}_i$, the approximation error can be expanded as follows

$$e_{\mathsf{a}_*}^2 = \left\| \sum (\lambda_i - \mathsf{a}_*) D_i \widehat{\mathbf{D}}_i \right\|^2 = \sum (\lambda_i - \mathsf{a}_*)^2 D_i^2 \quad \text{where} \quad \mathsf{a}_* = \sum \lambda_i D_i^2 \,, \tag{11}$$

where the second equality comes from the orthonormality of the basis $\widehat{\mathbf{D}}_i$. A few remarks are in order:

- As a standard Rayleigh quotient, the approximation error is actually zero when the deformation mode $\mathbf{D}$ coincides with one of the 5 eigenmodes $\widehat{\mathbf{D}}_i$ in (9). In particular, at the maximizing deformation mode $\widehat{\mathbf{D}}_{\max}$ the flow-fiber coupling factor a_* is maximum and the optimal scalar viscosity approximation is also perfect. This point can be verified in Fig. 4 (b), where at the UD orientation state $(a_1, a_2) = (1, 0)$ the approximation error is indeed zero for its maximizing uniaxial elongation mode.

- It can also be shown from (11) that the approximation error reaches its maximum value of $(\lambda_{\max} - \lambda_{\min})/2$ in the direction exactly between the minimizing and the maximizing eigen-deformation modes

$$\max(e_{\mathsf{a}_*}) = e_{\mathsf{a}_*}\left(\frac{\sqrt{2}}{2}(\widehat{\mathbf{D}}_{\min} \pm \widehat{\mathbf{D}}_{\max})\right) = \frac{\lambda_{\max} - \lambda_{\min}}{2}. \tag{12}$$

  In (12), either addition or subtraction will work, and note that multiple minimizing (resp. maximizing) eigenmodes corresponding to the same minimal (resp. maximal) eigenvalue may exist. It can be observed that the maximal approximation error is nothing but a rescaled numerical range of our coupling factor, see again Fig. 5 (b). Hence, while at the UD orientation state $(a_1, a_2) = (1, 0)$ the extent of anisotropy is maximal, it may also commit the highest approximation error (7) of $\frac{1}{3}$ as we reduce the 4th-order tensor to a scalar. For instance, for the typical fiber orientation state studied in Tab. 1, a maximal approximation error of about 0.21 can be obtained at a deformation mode $\widetilde{\mathbf{D}}$ that combines the maximizing general elongation and the shear flow in the 2-3 plane

$$\widetilde{\mathbf{D}} \approx \begin{bmatrix} 0.58 & 0 & 0 \\ 0 & -0.28 & 0.5 \\ 0 & 0.5 & -0.30 \end{bmatrix}.$$

  Luckily, for injection molding this kind of flow mode should not be frequent.

Remark 2. Note the *absolute* nature of the above approximation errors e_{η_*} and e_{a_*} in (5) and (7). A relative approximation error in the sense of $e_{\eta_*}/\|\mathrm{dev}(\mathbb{V}\mathbf{D})\|$ could also be defined but requires further mathematical development.

2.3. Fiber orientation and concentration models and implementation details

Other ingredients of our flow-fiber coupled injection simulation framework will be briefly discussed, since further improvements of these fiber evolution models themselves are beyond the scope of this paper. The computed orientation $\mathbf{a}$ and concentration ϕ will be simply "injected" into the optimal scalar viscosity model (6), via the dimensionless coupling factor a_* and the particle number N_p defined by (3).

Fiber orientation model. In this paper only the Reduced Strain Closure (RSC) fiber orientation model [43] will be used to compute the 2nd-order fiber orientation tensor. In addition to the interaction coefficient C_i that measures diffusion due to entanglement [21], the model introduces a reduction factor $0 < \kappa \leq 1$ that slows down fiber orientation rate in an objective way. Based on their respective simulation results, authors of [13, 18] found that flow-fiber coupling effects are more important when slow orientation kinetics are explicitly introduced into the fiber orientation model. The classical Folgar-Tucker model [21] simply predicts an orientation evolution too fast to benefit greatly from a fiber-dependent viscosity.

Fiber concentration model. The suspension balance model (SBM) implemented in Moldflow Insight 2019 Technology Preview [44] is used to compute a spatially varying fiber volume concentration ϕ that will feed the N_p expression (3). Also based on a micromechanical (homogenization) approach, the SBM is designed to capture shear-induced migration of fillers and will produce a non-uniform volume concentration that are also observable for injection molded parts [4]. The interested readers can refer to [45] for a recent review of this model. Nevertheless, such model is not yet popularized in injection molding simulations, probably because some theoretical improvements outlined in [46] are still awaited. Some recent successful attempts have been made in the community [47, 48] to validate the SBM against experimentally measured fiber

concentration distributions reported in the literature. Among the many physical parameters of the model, we will be mainly interested in two scalar parameters: the fiber equivalent radius R_{eq} that characterizes the size of fibers and a similar A parameter (maximum packing volume fraction) in the particle normal stress viscosity like in the N_{p} expression. The same value of A will be used in the SBM and in (3).

Implementation in the Moldflow API framework. The optimal scalar viscosity model (6) is implemented in the Moldflow Insight API framework [19], see [18]. Recall that in (6) the viscosity η refers to that of the unfilled matrix. Based on the assumption that rheological measurements on fiber-reinforced materials η_{MF} are conducted at high shear rates, in [18] a simple $\overline{a}_{11} \approx 1$ parameter is introduced to characterize the quasi-unidirectional fiber alignment $(a_1, a_2) = \left(\overline{a}_{11}, \frac{1}{2}(1 - \overline{a}_{11})\right)$ in such situations. Using (6), the viscosity of the suspending fluid η can be estimated by

$$\eta = \frac{\eta_{\text{MF}}}{1 + N_{\text{p}}(\overline{\phi})\overline{\mathsf{a}}_*}, \tag{13}$$

where $\overline{\mathsf{a}}_*$ is computed with such quasi-UD orientation states and the simple shear deformation mode. In this paper since fiber concentrations are assumed to be non-uniform in general, it is further assumed in (13) that the volume concentration is at its nominal value $\overline{\phi}$ when computing the particle number coefficient N_{p} using (3). Using (13), a non-dimensional viscosity scaling factor $\hat{\eta}$ can thus be introduced to compute effectively the optimal scalar viscosity (6) given the Moldflow viscosity

$$\eta_* = \hat{\eta} \cdot \eta_{\text{MF}} = \frac{1 + N_{\text{p}}\mathsf{a}_*}{1 + N_{\text{p}}(\overline{\phi})\overline{\mathsf{a}}_*}\eta_{\text{MF}}.$$

The scaling factor $\hat{\eta}$ characterizes the relative increase of decrease of the nominal viscosity η_{MF} due to the interaction between actual fiber orientation, concentration and deformation mode. Its variation with respect to the coupling factor a_* is indicated in Fig. 6 using the nominal parameters (volume concentration in particular) of the material considered. It can be seen that at the maximum coupling situation $\mathsf{a}_* = \frac{2}{3}$, a factor of 20 can be obtained compared to the standard fiber-independent viscosity. As in Fig. 2, the decrease of A slightly increases the coupling effect. Note that in the nominal concentration case, as N_{p} becomes larger, the scaling factor would converge to its maximal curve $\mathsf{a}_* \,/\, \overline{\mathsf{a}}_*$. Similar situation can also be found in [35].

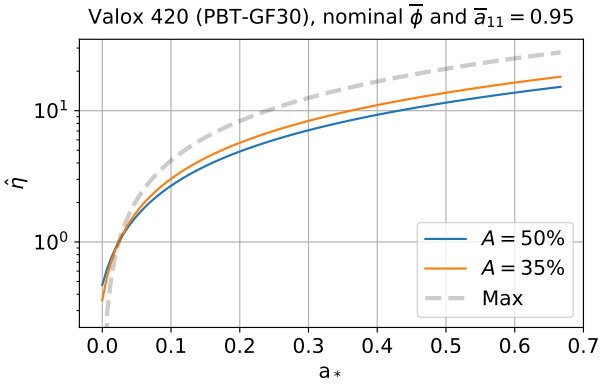

Figure 6: Viscosity scaling factor $\hat{\eta}$ as a function of a_* for two values of the A parameter, using the nominal material parameters of Valox 420.

As in our previous work [18] and similarly in [11, 13], a *weakly-coupled* approach is adopted to couple flow equations and fiber evolution. The coupling information (orientation and concentration into the proposed

viscosity model) is thus exchanged at one time-step delay. The obtained flow-fiber coupled injection molding simulation framework is extremely robust and efficient: no convergence issues have yet been found, and virtually nor significantly higher computational overhead compared to a standard uncoupled simulation. On a standard workstation (Intel Xeon 3.6 GHz, 16 GB of RAM, 4 cores, automatic parallelization), a typical simulation that will be discussed in Section 3 (1.2 million tetrahedral elements) requires approximately 1 hour 20 minutes for uncoupled simulations, and 1 hour 30 minutes for coupled ones.

3. Numerical simulations

3.1. Problem statement

The geometry and the measurement positions of the considered center-gated disk of total thickness $2H = 1.38\,\text{mm}$ are recalled in Fig. 7. In those experiments the disks were in fact only filled partially up to approximately 90% of the total radial flow length. Consequently the outer radius $r_{\text{out}} = 51.53\,\text{mm}$ of the incomplete disk is used for simulation and only the filling stage (without packing) is considered in this work. The melt is injected through a conic sprue of radius $r_{\text{in}} = 2.97\,\text{mm}$ at the junction with the disk.

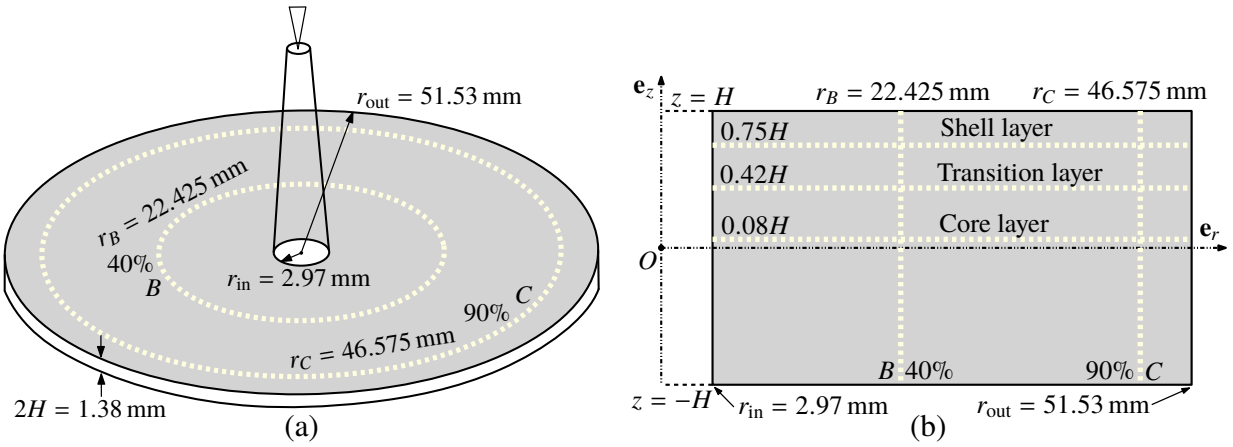

Figure 7: Geometrical parameters and measurement positions of the center gated plate: (a) 3d view with B and C two measurement radial positions along the thickness direction (b) cut view with three additional measurement height levels (shell, transition and core layers) along the radial direction.

The injection molding parameters used for experiments and our simulations are summarized in Tab. 2. An abundance of experimental fiber orientation / concentration measurements is available for this problem. In this paper for validation purposes, the gapwise (z) variation of fiber orientation at 2 radial positions reported in [24, 28] are considered: $r_B = 22.425\,\text{mm}$ (40% of the flow length $R = r_{\text{out}} - r_{\text{in}}$) corresponding to the lubrication region, and $r_C = 46.575\,\text{mm}$ (90% of R) in the near-end-of-fill region. In addition, fiber orientation measured at 3 height levels along the radius (r) direction are also used: the shell layer at $z = 0.75H$, the transition layer $z = 0.42H$ and the core layer $z = 0.08H$, cf. [10] and Fig. 7 (b). Finally, the fiber volume concentration measurements of [24] will also be compared with our simulation predictions: one at the flow length center ($r = 27.25\,\text{mm}$), and the other in the entry region.

The injected material is a 30 wt% short glass fiber filled polybutylene terephthalate (PBT-GF30) under the trade name Valox 420. For their simulations the authors of [10, 28] used a Newtonian viscosity model $\eta = 350\,\text{Pa}\cdot\text{s}$ according to the experimental findings in the shear-rate range from $10^{-1}\,1/\text{s}$ to $10^{2}\,1/\text{s}$. In this work a shear-rate dependent viscosity η_{MF} stored in the Moldflow database is used to estimate the viscosity

Table 2: Injection molding parameters.

Injection time	Melt temperature	Mold temperature
1 s	260 °C	90 °C

of the unfilled matrix using (13). We find that the Moldflow viscosity η_{MF} agrees well with the reported constant viscosity value within the range, and presents further shear-thinning phenomenon at higher shear rates. Note also that a temperature-dependence is also included in η_{MF} under Moldflow Insight along with the computation of the temperature field T at every time step as the flow advances. In [10, 28] however, an isothermal condition is assumed.

The parameters for the fiber orientation and concentration models are summarized in Tab. 3 along with other parameters in our flow-fiber coupled simulation framework. Note that the default equivalent radius parameter $R_{\mathrm{eq}} = 0.02\,\mathrm{mm}$ agrees fairly well with the experimental data [24] which gives 0.022 mm. Using $A = 50\%$, the resulting particle number N_{p} is equal to 47, larger than that considered in [10]. The RSC parameters are chosen via a systematic parametric optimization procedure that will be described in a separate paper. Note that the values used are close to those fitted with rheological experiments and used in [10, 28, 43].

Table 3: Parameters of the flow-fiber coupled simulation framework used in this work.

Fiber orientation	Fiber concentration	Optimal scalar viscosity
$(C_{\mathrm{i}}, \kappa) = (0.015, 0.2)$	$R_{\mathrm{eq}} = 0.02\,\mathrm{mm}$, $A = 50\%$	$A = 50\%$ for N_{p}, $\overline{a}_{11} = 0.95$ in (13)

Remark 3. In this section, "uncoupled" simulation refers to standard injection simulations where fiber-independent viscosity η_{MF} is used; "coupled" simulation refers to the simulation framework described in Section 2 via the optimal scalar viscosity (6). When non-uniform fiber concentration effects *are not* considered, the nominal fiber concentration value (30 wt%) is used for N_{p}.

3.2. Settings and post-processing of numerical simulations

The simulations are performed with Moldflow Insight 2019 Technology Preview [44]. From a computational point of view, the sprue is meshed with beam elements and the center-gated disk is spatially discretized with a non-structured surface mesh with a typical mesh size $h \approx 1$ mm, see Fig. 8 (a). With a 3-dimensional modeling approach, 16 layers of tetrahedrons are generated in the thickness z direction and totally we have approximately 1.2 million elements. We have verified that a refined mesh with 20 layers of tetrahedrons does not lead to much variations in the simulation results. Interested readers can refer to the supplementary material available online.

In [10, 28], the numerical simulations are conducted on an effective 2-dimensional domain where axisymmetry is taken into account directly into the formulation. Due to the 3-dimensional nature of our analysis and the non-structured mesh, the obtained simulation results are not perfectly axisymmetric with respect to the z-axis. We believe that these numerical variabilities can be justified since they can represent various physical imperfections or uncertainties during the experiments: geometrical, material, injection settings, etc. To quantify and extract information from these variabilities, an angular averaging procedure is

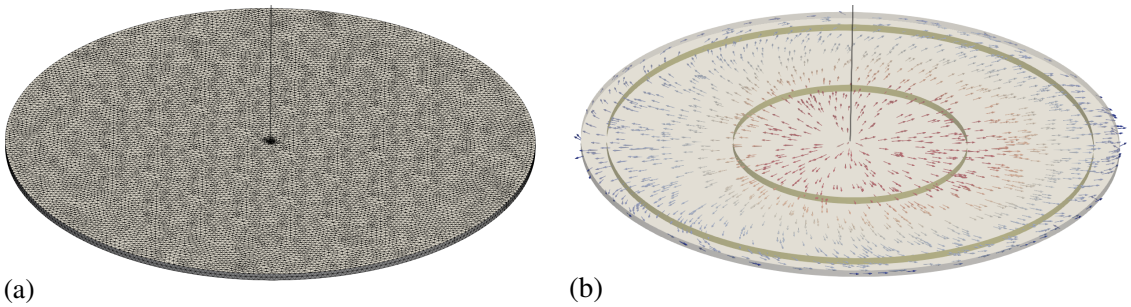

Figure 8: (a) Non-structured surface mesh used for simulations; (b) qualitative illustration of the velocity field on the midplane of the disk at the end of fill, with indications of two radial B / C measurement "cylindrical rings" in yellow.

used to post-process the simulation results: velocity, fiber orientation and concentration in particular. In Fig. 8 (b), a qualitative illustration of the velocity field on the midplane of the disk at the end of fill is presented. The following formula is used to obtain the *averaged* gapwise radial velocity $\overline{v}_r(z)$ at two measurement positions B and C illustrated by two "cylindrical rings"

$$\overline{v}_r(z) = \frac{1}{2\pi}\int_0^{2\pi} v_r(\theta, z)\,\mathrm{d}\theta \quad \text{at } r = r_B \text{ or } r_C\,.$$

Since such advanced post-processing could not yet be performed under Moldflow, the simulation results are exported via an in-house software (Promold Moldflow Results Exporter) to a format readable by ParaView [49], a powerful open-source visualization application. The obtained averaged typical v_r as a function of the normalized thickness z/H is presented in Fig. 9 (a). The angular variability can be quantified using respectively the 10% quantile as the lower bound and the 90% quantile as the upper bound, both indicated by shaded regions in the figure. It can be seen that a maximum angular variability of about 30% can produce on the core layer.

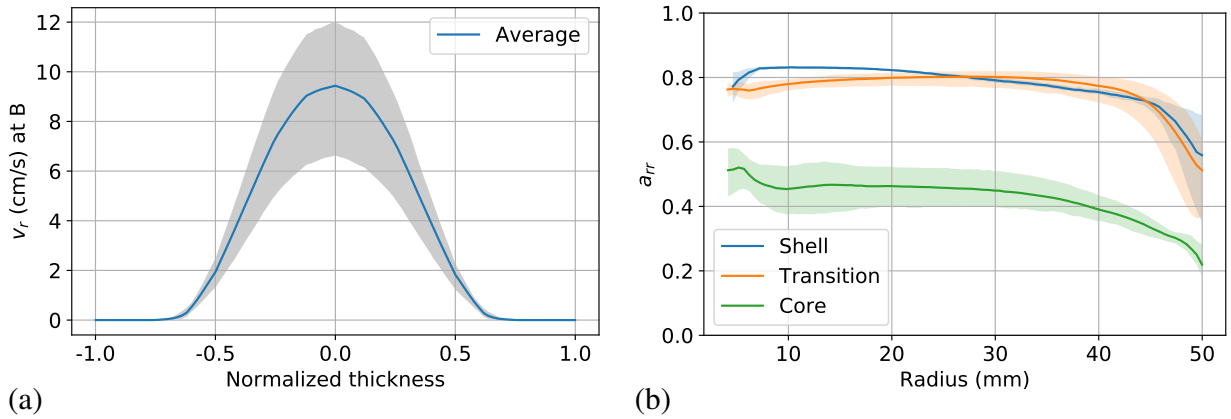

Figure 9: Angular averaged (a) gapwise velocity v_r and (b) fiber orientation a_{rr} along the radius direction, with angular variability indicated by shaded regions.

A similar expression is used to compute an angular averaged result along the radial direction on one of the three height levels in Fig. 7 (b). For example, the radial variation of the radial fiber orientation a_{rr} on the shell, transition and core layers is shown in Fig. 9 (b). The angular variability is maximum in the core,

but also at the end of fill on the shell / transition layers. In the subsequent presentation, only the angular averaged result will be presented for readability concerns.

3.3. Preliminary verification analyses of numerical parameters

Before any confrontation with experimental results, we propose to verify the sensibilities of the simulation results with respect to various numerical parameters. We will be mainly interested in two parameters: (a) the initial inlet fiber orientation condition and (b) the maximum time-step increment Δt. Only results will be reported here. Interested readers can refer to the supplementary material for the simulation data.

Three inlet conditions are considered: the default option where the "fibers aligned at skin / random at the core" orientation is prescribed at the junction between the sprue and the disk, the condition where the previous orientation is imposed at the injection point and finally the case where the "fibers aligned at skin / transverse at core" orientation is assumed at the gate. Based on the simulation results, it can be concluded that different inlet conditions will indeed induce differences in fiber orientation especially near the gate. However as have been also observed by [17, 50], this effect will be rapidly washed out as the flow advances. A correct prediction of fiber orientation in the entry region may strongly depend on the exact runner system design and the pre-processing of the fiber-reinforced melt. This is the reason why in this paper the other fiber orientation measurement radius $r_A = 7.8$ mm just after the gate reported in [24] is not considered. In the subsequent simulations, only results obtained with the default inlet option will be reported.

A *weakly-coupling* approach is adopted in our simulation framework, hence it is essential to guarantee a converging behavior when reducing the maximum time-step increment parameter Δt with flow-fiber coupling. Our simulation data show little sensitivities as also observed in our previous work [18]. The default value of $\Delta t = 4\%$ may be sufficient to obtain a converged solution.

3.4. Effects of flow-fiber coupling and non-uniform concentration

In Fig. 10 (a), the simulations produce a correct skin-shell-core structure in fiber orientation at the measurement radius B, and a good agreement with experiment apart from two extremely aligned values measured on the shell layer.

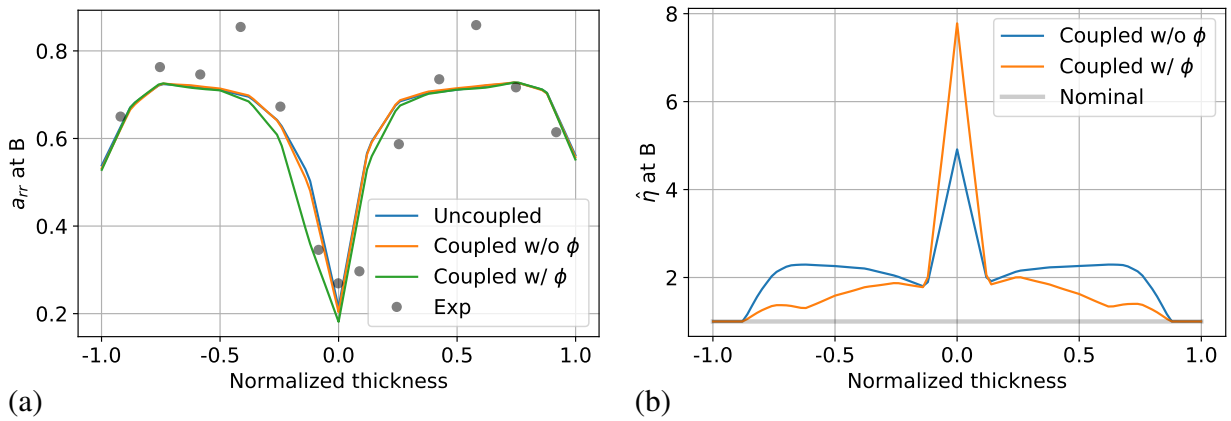

Figure 10: (a) Radial fiber orientation a_{rr} at B; (b) viscosity scaling factor at B.

The use of flow-flow coupling further decreases orientation kinetics especially in the core, similar to what have been observed in [10]. The coupling effect is more obvious when non-uniform fiber concentration is considered (labeled "coupled w/ ϕ"). This is confirmed in Fig. 10 (b), where the viscosity scaling factor presents a higher value in the core than the case when the nominal fiber concentration value is used (labeled

"coupled w/o ϕ"). A slight drop of $\hat{\eta}$ is also observed on the shell layer. The reason for all these differences in fiber orientation and viscosity when coupling is considered comes from a non-uniform fiber concentration in the thickness direction, illustrated in Fig. 11 (a) for the flow length center radius. The experimental data are indicated by a shaded region corresponding to different methods deployed in [24].

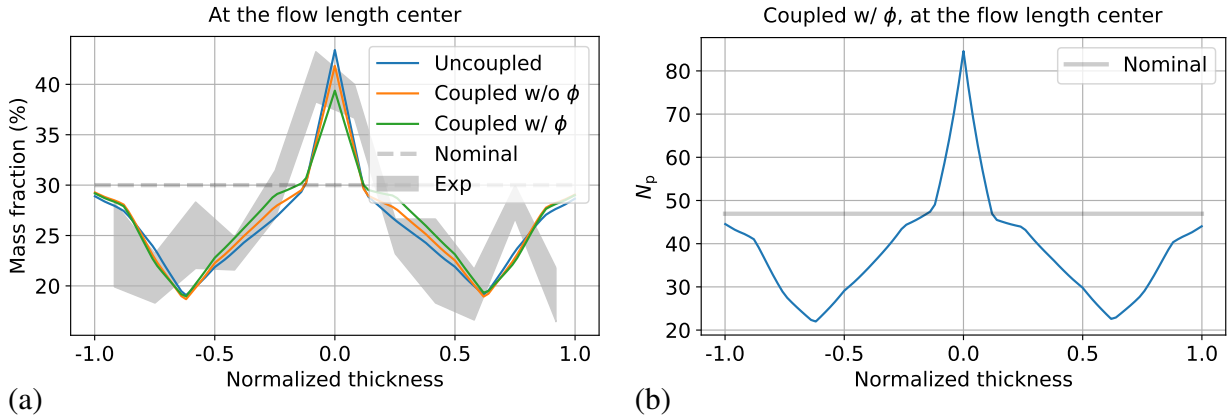

Figure 11: (a) Mass fraction at the flow length center with or without flow-fiber coupling; (b) corresponding N_p parameter with coupling and non-uniform fiber concentration effects.

It can be seen that both the uncoupled and coupled simulations deliver a quantitatively satisfying fiber concentration distribution. Due to the newly introduced flow – fiber orientation / concentration two-way coupling (see Fig. 1), the exact concentration distribution can be altered by the coupling and vice versa. In this particular case, coupling seems to slightly further improve agreement with the experimental result. Due to shear-induced migrations, there are indeed more fibers present in the core than on the shell layer, where the shear rate is higher. This particular concentration profile contributes hence to a non-uniform flow-fiber coupling effect via the N_p parameter according to (3), see Fig. 11 (b). For comparison the nominal value of N_p is also indicated. On the one hand, the coupling effect is thus higher in the core, due to a higher fiber concentration compared to the nominal case. On the other hand, due to a lower mass fraction on the shell layer, the coupling effect is over-estimated with the nominal concentration value.

The radial fiber orientation a_{rr} along the radius direction is analyzed in Fig. 12 for the transition and the core layers. Contrary to [10], a short decrease of a_{rr} is not observed near the gate for the transition layer. This should probably due to a different runner system and inlet conditions, which should be washed out afterwards. The subsequent agreement with experimental results is excellent on the transition layer. Similar satisfying predictions can also be found on the shell layer. Our 3-dimensional analysis also predicts a correct gradually decreasing radial fiber orientation as the flow advances for the three height levels. This illustrates again the importance of fountain flows in an injection molding simulation, cf. [10, 11].

On the one hand, the flow-fiber coupling does not lead to much variations of fiber orientation on the shear and transition layers governed by dominant shear components, see similar results reported in [10, 18]. On the other hand, contrary to [10], we do observe a noticeable decrease of a_{rr} on the core layer when non-uniform concentration effects are also included during coupling, leading to a better agreement with experiments. However, when the nominal concentration value is used, the improvement is modest conforming to the gapwise representation seen in Fig. 10 (a). This illustrates the importance of considering such spatially-varying fiber concentration.

Finally, to better explore the global coupling effect, the radial velocity v_r and the viscosity scaling factor $\hat{\eta}$ on the core layer are presented in Fig. 13. The steady-state analytical radial velocity solution for

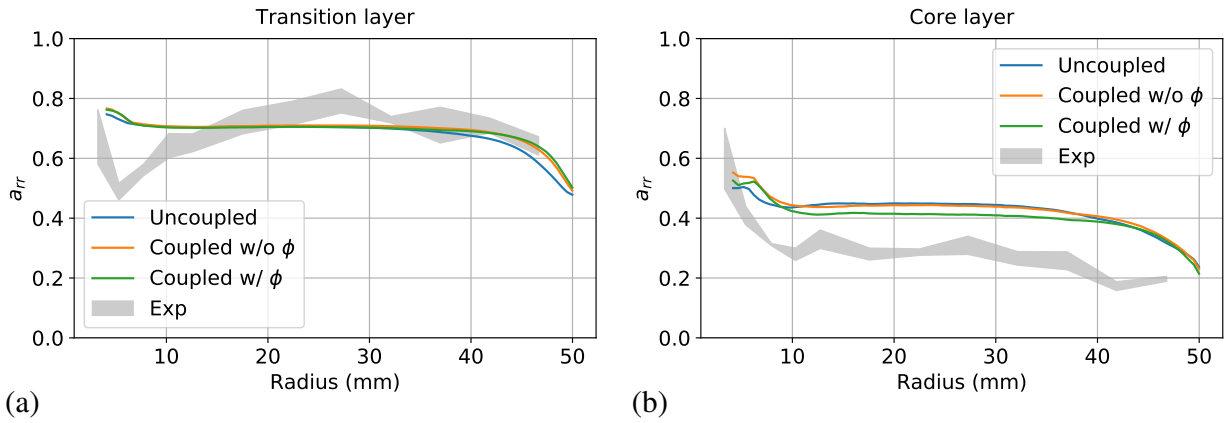

Figure 12: Radial fiber orientation a_{rr} in the (a) transition and (b) core layers, with or without flow-fiber coupling.

an isothermal Newtonian fluid indicated in [28] is also shown. The theoretical curve matches well with the uncoupled simulation especially in the lubrication region, indicating a quasi-Newtonian behavior. The curves then diverge near the end of the flow path due to boundary effects and fountain flows [11]. Similar to [10], when the nominal concentration value is used, the velocity in the core is even slightly larger in the coupled simulation compared to the uncoupled case. A visible slowed-down velocity can only be observed when non-uniform concentration effects are considered. The effect of coupling is also more obvious near the gate due to stronger extensional flows. As can be seen from Fig. 13 (b), the scaling factor is higher throughout the radial direction when such effects are taken into account, contributing to a more important flow-fiber coupling.

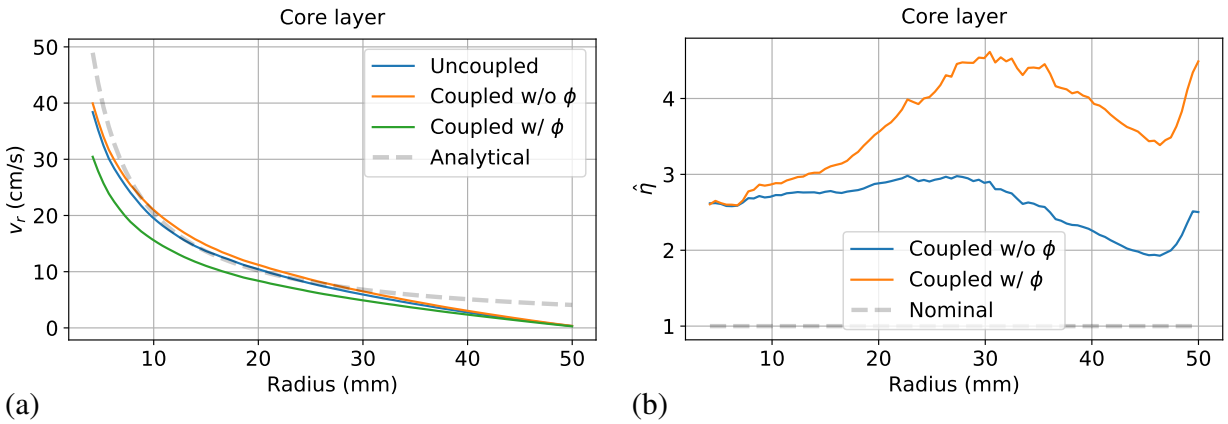

Figure 13: Radial velocity (a) and viscosity scaling factor (b) on the core layer, with or without flow-fiber coupling.

3.5. Effect of the A parameter on coupling

Recall that a decrease of the A parameter that is both present in the SBM and in the N_p parameter will increase the coupling effect. As can be seen from Figs. 2 and 6, the increase in N_p and $\hat{\eta}$ is modest when the *nominal fiber concentration* is considered. Hence, we do not observe any visible differences in fiber orientation predictions in such case.

However, when *non-uniform fiber concentration effects* are taken into account during flow-fiber coupling, the effect of A parameter is more important. This can be expected from Fig. 2 since with a smaller A the N_p parameter predicts a much higher value especially at large mass fractions, *i.e.* in the core. In Fig. 14 (a), the radial fiber orientation a_{rr} on the core layer is presented for two values of A. For $A = 35\%$, the prediction is further improved and can even match the experimental data when angular variabilities are accounted for. In comparison with uncoupled or "coupled w/o ϕ" simulations in Fig. 12 (b), the effect of non-uniform concentration becomes more obvious. Note that the fiber evolution on the transitions layer (but also for the shell layer) is not impacted compared to Fig. 12 (a).

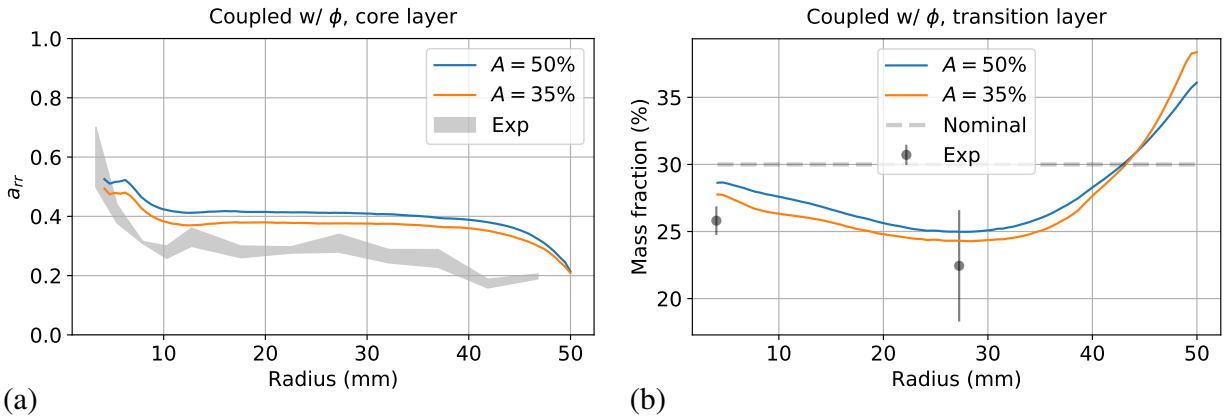

Figure 14: Flow-fiber coupling with non-uniform concentration effects for two values of A: (a) radial fiber orientation a_{rr} on the core layer; (b) mass fraction on the transition layer.

Since this parameter also conditions fiber concentration prediction, the mass fraction distribution along the radius direction on the transition layer is also shown in Fig. 14 (b). The simulation result is improved using $A = 35\%$ compared with the experimental measurements, and showcases a non-monotonic migration behavior along the flow path, probably due to the competition between shear and elongational flows during convection.

Finally, the effect of the A parameter can also be perceived by the gapwise radial velocity distribution, see Fig. 15 at the measurement radius C. As can be expected from Fig. 13 (a), when non-uniform concentration effects are introduced, the velocity profile is blunted in the core compared with the uncoupled Newtonian-like parabolic profile. Similar phenomenon has already been reported recently for the optimal scalar viscosity model in [13, 18]. As above, the use of a smaller A value enhances the coupling effect and further slows down flow kinematics in the center.

4. Conclusions and future work

A novel flow-fiber coupled injection molding simulation framework, with the consideration of non-uniform fiber concentration effects, has been proposed in Section 2. As suggested by [18], further theoretical analyses are carried out to better understand the optimal scalar viscosity model (6) previously developed by the authors. Some useful properties of the scalar model can be obtained through spectral decomposition of the (deviatoric) 4th-order viscosity tensor. From the point of view of rheological modeling, the fiber-induced anisotropy is correctly captured by the scalar variational (minimization) principle. The approximation error induced in such process is shown to be bounded and can also be quantified for arbitrary orientation states. The proposed optimal scalar viscosity model can thus be used with confidence from a theoretical point of

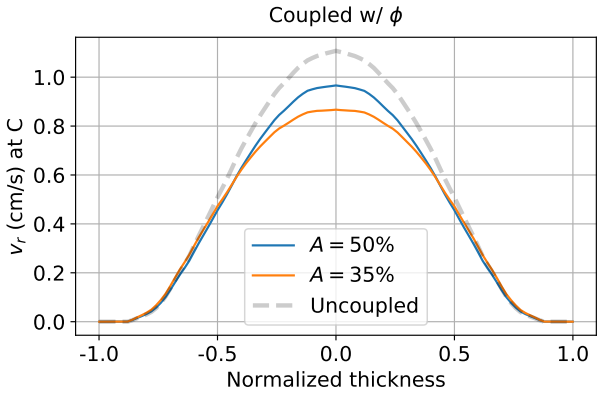

Figure 15: Gapwise radial velocity v_r at the measurement radius C with coupling and non-uniform concentration effects for two values of A.

view. The scalar nature further facilitates its implementation in commercial or academic flow simulation software.

The well-documented center-gated disk problem [10, 24, 28] is revisited with a focus on fiber-flow coupling and shear-induced non-uniform fiber concentration effects. On the one hand, probably due to the slenderness of the disk (here the thickness equals 1.38 mm, while in our previous work the thickness was larger than 3 mm) and a relatively moderate fiber content (30 wt%, whereas before we considered 50 wt%), the standard flow-fiber coupling with the nominal fiber concentration value does not bring noticeable improvements to fiber orientation predictions. This observation agrees with some previous attempts [10, 11], conforming to the dimensional analysis [15]. On the other hand, our new numerical simulations indicate that the consideration of a non-uniform fiber concentration may further enhance the previously underestimated flow-fiber coupling effect and eventually improve fiber orientation predictions. With well-chosen modeling parameters of the orientation, concentration and coupling parameters, our model is capable of predicting qualitatively correct radial fiber orientation evolution that also match the experimental measurements on different height levels.

Along with [27], this work has introduced a new paradigm for injection molding simulations, where two previously independent fiber evolution models (orientation via the RSC model and concentration via the SBM) are *two-way* coupled with the flow equations during the filling stage via the proposed fiber-dependent optimal scalar viscosity model. From a simulation point of view, this multiphysics coupling guarantees a more accurate rheological modeling of fiber suspensions, which in return leads to a better characterization of the complex non-Newtonian flows and fiber microstructural properties induced by the process. It brings out some additional interesting future research directions besides those raised previously in our previous work:

- Analytical or semi-analytical investigation of flow-fiber multiphysics coupling for some academic example problems. Under some simplifying hypotheses, these mathematical studies could for instance provide a better theoretical understanding of the coupling effect on orientation and concentration.

- Indirect coupling between fiber concentration and fiber orientation. Their *individual* and *explicit* coupling with the flow should automatically induce an *implicit* coupling relation between themselves, see Fig. 1. For instance, an increase of the volume concentration leads to an increased viscosity which may reduce the shear rate. Consequently it could further slow down fiber orientation kinetics. This scenario qualitatively matches some previous experimental [21] and analytical [51] results, while

contradicts other findings such as [16]. This concentration-dependence of orientation could be taken into account without flow-fiber coupling, for instance via an empirical relation $C_i = C_i(\phi)$. It may be interesting from a theoretical point of view to investigate such dependence within the proposed flow-fiber coupling framework.

Supplementary material

Some results of the preliminary numerical sensitivity analyses can be found at https://bitbucket.org/litianyi/center_gated_disk.

Acknowledgment

The authors are grateful for Dr. Franco Costa for having suggested considering non-uniform fiber concentration effects for flow-fiber coupling during an informal discussion. This research is funded by the Région Île-de-France through the THERMOFIP research program (Pôle MOV'EO Convention 1709965). The Moldflow API simulations presented in this paper could not be performed without the generous and unconditional help of Alain Benchissou from APLICIT.

Competing interests

The authors declare that they have no competing interests.

References

[1] M. Gupta, K. K. Wang, Fiber orientation and mechanical properties of short-fiber-reinforced injection-molded composites: Simulated and experimental results, Polymer Composites 14 (1993) 367–382. doi:10.1002/pc.750140503.

[2] M. F. Arif, N. Saintier, F. Meraghni, J. Fitoussi, Y. Chemisky, G. Robert, Multiscale fatigue damage characterization in short glass fiber reinforced polyamide-66, Composites Part B: Engineering 61 (2014) 55–65.

[3] H. Rolland, N. Saintier, G. Robert, Damage mechanisms in short glass fibre reinforced thermoplastic during in situ microtomography tensile tests, Composites Part B: Engineering 90 (2016) 365–377.

[4] T. D. Papathanasiou, Flow-induced alignment in injection molding of fiber-reinforced polymer composites, in: T. D. Papthanasiou, D. C. Guell (Eds.), Flow-induced alignment in composite materials, Woodhead Publishing Cambridge, 1997.

[5] N. Phan-Thien, R. Zheng, Macroscopic modelling of the evolution of a fibre orientation during flow, in: T. D. Papthanasiou, D. C. Guell (Eds.), Flow-induced alignment in composite materials, Woodhead Publishing Cambridge, 1997.

[6] J. Azaiez, K. Chiba, F. Chinesta, A. Poitou, State-of-the-art on numerical simulation of fiber-reinforced thermoplastic forming processes, Archives of Computational Methods in Engineering 9 (2002) 141–198.

[7] B. E. Verweyst, C. L. Tucker III, Fiber Suspensions in Complex Geometries: Flow/Orientation Coupling, The Canadian Journal of Chemical Engineering 80 (2002) 1093–1106. doi:10.1002/cjce.5450800611.

[8] D. H. Chung, T. H. Kwon, Numerical studies of fiber suspensions in an axisymmetric radial diverging flow: the effects of modeling and numerical assumptions, Journal of Non-Newtonian Fluid Mechanics 107 (2002) 67–96.

[9] J. M. Park, T. H. Kwon, Nonisothermal transient filling simulation of fiber suspended viscoelastic liquid in a center-gated disk, Polymer Composites 32 (2011) 427–437.

[10] S. M. Mazahir, G. M. Vélez-García, P. Wapperom, D. Baird, Evolution of fibre orientation in radial direction in a center-gated disk: Experiments and simulation, Composites Part A: Applied Science and Manufacturing 51 (2013) 108–117.

[11] S. M. Mazahir, G. M. Vélez-García, P. Wapperom, D. Baird, Fiber orientation in the frontal region of a center-gated disk: Experiments and simulation, Journal of Non-Newtonian Fluid Mechanics 216 (2015) 31–44.

[12] G. Lambert, P. Wapperom, D. Baird, Obtaining short-fiber orientation model parameters using non-lubricated squeeze flow, Physics of Fluids 29 (2017) 121608.

[13] A. J. Favaloro, H.-C. Tseng, R. B. Pipes, A new anisotropic viscous constitutive model for composites molding simulation, Composites Part A: Applied Science and Manufacturing 115 (2018) 112–122. doi:10.1016/j.compositesa.2018.09.022.

[14] D. E. Sommer, A. J. Favaloro, R. B. Pipes, Coupling anisotropic viscosity and fiber orientation in applications to squeeze flow, Journal of Rheology 62 (2018) 669–679. doi:10.1122/1.5013098.
[15] C. L. Tucker III, Flow regimes for fiber suspensions in narrow gaps, Journal of Non-Newtonian Fluid Mechanics 39 (1991) 239–268.
[16] J. K. Jørgensen, E. Andreassen, D. Salaberger, The effect of fiber concentration on fiber orientation in injection molded film gated rectangular plates, Polymer Composites (2017).
[17] S. Kleindel, D. Salaberger, R. Eder, H. Schretter, C. Hochenauer, Prediction and validation of short fiber orientation in a complex injection molded part with chunky geometry, International Polymer Processing 30 (2015) 366–380.
[18] T. Li, J.-F. Luyé, Flow-fiber coupled viscosity in injection molding simulations of short fiber reinforced thermoplastics, International Polymer Processing (2018). URL: https://hal.archives-ouvertes.fr/hal-01683052.
[19] F. Costa, P. Cook, D. Pickett, A framework for viscosity model research in injection molding simulation, including pressure and fiber orientation dependence, in: SPE ANTEC Conference, 2015.
[20] G. B. Jeffery, The motion of ellipsoidal particles immersed in a viscous fluid, in: Proceedings of the royal society of London A: Mathematical, physical and engineering sciences, volume 102, The Royal Society, 1922, pp. 161–179.
[21] F. Folgar, C. L. Tucker III, Orientation behavior of fibers in concentrated suspensions, Journal of Reinforced Plastics and Composites 3 (1984) 98–119.
[22] K. Chiba, K. Yasuda, K. Nakamura, Numerical solution of fiber suspension flow through a parallel plate channel by coupling flow field with fiber orientation distribution, Journal of Non-Newtonian Fluid Mechanics 99 (2001) 145–157. doi:10.1016/s0377-0257(01)00118-5.
[23] S. Toll, P.-O. Andersson, Microstructure of long- and short-fiber reinforced injection molded polyamide, Polymer Composites 14 (1993) 116–125. doi:10.1002/pc.750140205.
[24] G. M. Vélez-García, P. Wapperom, D. G. Baird, A. O. Aning, V. Kunc, Unambiguous orientation in short fiber composites over small sampling area in a center-gated disk, Composites Part A: Applied Science and Manufacturing 43 (2012) 104–113.
[25] V. Perumal, R. K. Gupta, S. N. Bhattacharya, F. S. Costa, Fiber orientation prediction in Nylon-6 glass fiber composites using transient rheology and 3-dimensional X-ray computed tomography, Polymer Composites (2018). doi:10.1002/pc.24700.
[26] S. Goris, T. A. Osswald, Process-induced fiber matrix separation in long fiber-reinforced thermoplastics, Composites Part A: Applied Science and Manufacturing 105 (2018) 321–333.
[27] V. Perumal, R. K. Gupta, S. N. Bhattacharya, F. S. Costa, S. Kashi, Modelling stress response of glass-fibre composites during shear flow using 3-dimensional fiber orientation evolution and fibre migration data, in: 18th European Conference on Composite Materials, 2018.
[28] G. M. Vélez-García, S. M. Mazahir, P. Wapperom, D. G. Baird, Simulation of injection molding using a model with delayed fiber orientation, International Polymer Processing 26 (2011) 331–339. doi:10.3139/217.2478.
[29] G. G. Lipscomb, M. M. Denn, D. U. Hur, D. V. Boger, The flow of fiber suspensions in complex geometries, Journal of Non-Newtonian Fluid Mechanics 26 (1988) 297–325. doi:10.1016/0377-0257(88)80023-5.
[30] N. Phan-Thien, A. Graham, A new constitutive model for fibre suspensions: flow past a sphere, Rheologica acta 30 (1991) 44–57.
[31] S. G. Advani, C. L. Tucker III, The use of tensors to describe and predict fiber orientation in short fiber composites, Journal of Rheology 31 (1987) 751–784.
[32] J. L. Ericksen, Anisotropic fluids, Archive for Rational Mechanics and Analysis 4 (1959) 231.
[33] S. T. Chung, T. H. Kwon, Coupled analysis of injection molding filling and fiber orientation, including in-plane velocity gradient effect, Polymer Composites 17 (1996) 859–872. doi:10.1002/pc.10679.
[34] M. M. Cross, Rheology of non-newtonian fluids: A new flow equation for pseudoplastic systems, Journal of Colloid Science 20 (1965) 417–437. doi:10.1016/0095-8522(65)90022-x.
[35] A. J. Favaloro, Rheological Behavior and Manufacturing Simulation of Prepreg Platelet Molding Systems, Ph.D. thesis, Purdue University, 2017.
[36] B. E. VerWeyst, Numerical predictions of flow-induced fiber orientation in three-dimensional geometries, Ph.D. thesis, University of Illinois at Urbana-Champaign, 1998.
[37] D. H. Chung, T. H. Kwon, Invariant-based optimal fitting closure approximation for the numerical prediction of flow-induced fiber orientation, Journal of Rheology 46 (2002) 169–194.
[38] A. Redjeb, P. Laure, L. Silva, M. Vincent, T. Coupez, Numerical simulation of fiber orientation in injection molding process, in: 21st Annual meeting of the Polymer Processing Society, 2005.
[39] H. M. Laun, Orientation effects and rheology of short glass fiber-reinforced thermoplastics, Colloid & Polymer Science 262 (1984) 257–269.
[40] J. S. Cintra Jr, C. L. Tucker III, Orthotropic closure approximations for flow-induced fiber orientation, Journal of Rheology 39 (1995) 1095–1122.
[41] S. I. Ranganathan, M. Ostoja-Starzewski, Universal elastic anisotropy index, Physical Review Letters 101 (2008). doi:10.

1103/physrevlett.101.055504.
[42] M. Moakher, A. N. Norris, The closest elastic tensor of arbitrary symmetry to an elasticity tensor of lower symmetry, Journal of Elasticity 85 (2006) 215–263. doi:10.1007/s10659-006-9082-0.
[43] J. Wang, J. F. O'Gara, C. L. Tucker III, An objective model for slow orientation kinetics in concentrated fiber suspensions: Theory and rheological evidence, Journal of Rheology 52 (2008) 1179–1200. doi:10.1122/1.2946437.
[44] Autodesk, Autodesk Moldflow 2019 Technology Preview: What is New, 2018.
[45] J. F. Morris, A review of microstructure in concentrated suspensions and its implications for rheology and bulk flow, Rheologica acta 48 (2009) 909–923.
[46] P. R. Nott, E. Guazzelli, O. Pouliquen, The suspension balance model revisited, Physics of Fluids 23 (2011) 043304. doi:10.1063/1.3570921.
[47] F. Costa, Autodesk Moldflow Insight: Solver Enhancements and Research Directions, in: Benelux Autodesk Moldflow User Meeting, 2016.
[48] H.-C. Tseng, R.-Y. Chang, C.-H. Hsu, Predictions of fiber concentration in injection molding simulation of fiber-reinforced composites, Journal of Thermoplastic Composite Materials (2017). doi:10.1177/0892705717738302.
[49] U. Ayachit, The ParaView Guide, Kitware Inc., 2018.
[50] J. Wang, P. Cook, A. Bakharev, F. Costa, D. Astbury, Prediction of fiber orientation in injection-molded parts using three-dimensional simulations, AIP Conference Proceedings 1713 (2016) 40007. doi:10.1063/1.4942272.
[51] N. Phan-Thien, X.-J. Fan, R. I. Tanner, R. Zheng, Folgar-Tucker constant for a fibre suspension in a Newtonian fluid, Journal of Non-Newtonian Fluid Mechanics 103 (2002) 251–260. doi:10.1016/s0377-0257(02)00006-x.